



# Ultrasensitive and accurate diagnosis of urothelial cancer by plasmonic AuNRs-enhanced fluorescence of near-infrared Ag<sub>2</sub>S quantum dots

Dong Zhang, Cai-Ping Ding, Xiao-Yue Zheng, Jia-Zhou Ye, Zi-Hai Chen, Jian-Hua Li, Ze-Jun Yan\* , Jun-Hui Jiang, You-Ju Huang\* 

Received: 28 February 2022 / Revised: 3 March 2022 / Accepted: 6 March 2022 / Published online: 1 September 2022  
© Youke Publishing Co., Ltd. 2022

**Abstract** Urothelial carcinoma (UC) is a common malignant tumor in the urinary system with high recurrence rate and low survival rate 5 years after surgery. At present, imaging examination and other diagnostic methods have some shortcomings such as invasiveness and non-specificity. Therefore, it is urgent to develop a simple, rapid, noninvasive, highly sensitive and highly specific strategy to diagnose UC. Herein, a high-performance fluorescence sensor was constructed by the plasmonic gold nanorods (AuNRs)-enhanced near-infrared (NIR) fluorescence of silver sulfide quantum dots (Ag<sub>2</sub>S QDs). The designed

sensor can be used for the fast and accurate detection of small molecule single-transmembrane protein (FXVD3), which is overexpressed in 90% of ureteral cancers and 84% of high-grade bladder cancers. Due to its high specificity, the NIR fluorescence sensor achieves the detection of FXVD3 in the range of 0.25–150 ng·ml<sup>-1</sup> with a detection limit of 0.2 ng·ml<sup>-1</sup>. Importantly, it also can be used for accurate diagnosis of FXVD3 in the urine of patients with relevant cancers, and the results are consistent with clinical cystoscopy and pathological analysis. The proposed fluorescence sensor provides a simple, ultrasensitive, reliable method for UC screening, tumor-grade classification and postoperative monitoring and will have great potential for clinical applications.

Dong Zhang and Cai-Ping Ding have contributed equally to this work.

**Supplementary Information** The online version contains supplementary material available at <https://doi.org/10.1007/s12598-022-02074-2>.

D. Zhang, Z.-J. Yan\*, J.-H. Jiang  
Department of Urology & Nephrology, Ningbo First Hospital,  
The Affiliated Hospital of Zhejiang University, Ningbo 315000,  
China  
e-mail: yanzejun2000@sina.com

C.-P. Ding, X.-Y. Zheng, J.-Z. Ye, Y.-J. Huang\*  
College of Material, Chemistry and Chemical Engineering, Key  
Laboratory of Organosilicon Chemistry and Material  
Technology, Ministry of Education, Hangzhou Normal  
University, Hangzhou 311121, China  
e-mail: yjhuang@hznu.edu.cn

Z.-H. Chen  
Anhui Shenghaitang Traditional Chinese Medicine Decoction  
Pieces Co., Ltd, Bozhou 236800, China

J.-H. Li  
Anhui Topway Testing Services Co., Ltd., Xuancheng Economic  
and Technological Development Zone, Xuancheng 242000,  
China

**Keywords** Urothelial carcinoma; FXVD3; Plasmonic enhanced fluorescence; Ultrasensitive; Accurate diagnosis

## 1 Introduction

Urothelial carcinoma (UC) is a common malignant tumor in the urinary system, including bladder tumor and upper urinary tract urothelial carcinoma (UTUC). Bladder cancer accounts for 90%–95% of cases, and UTUC (ureteral and pelvic cancers) accounts for about 5%–10% [1]. Of these, non-muscle invasive bladder cancer (NMIBC) accounts for 75% of bladder cancers and muscle invasive bladder cancer (MIBC) accounts for 25% of bladder cancers [2]. Transurethral resection of bladder tumor (TURBT) is the gold standard for the treatment of NMIBC [3]. However, according to the European Association of Urology (EAU) guidelines, 31%–78% of patients produce tumor recurrence within 5 years after surgery and require repeat or multiple



TURBT treatments, and 0.8%–45% of patients progress to MIBC due to unrecognized tumor recurrence [4, 5]. The 5-year survival rate for MIBC is only 46%–63%, and up to 90% for NMIBC [4, 5]. The main reason is that MIBC tumors are more malignant and have a worse prognosis, with approximately 30%–60% of patients having tumor infiltration or even invasion of surrounding tissues at the time of initial presentation [6, 7]. Therefore, early diagnosis and treatment are crucial for patients with UC and will improve their over-all survival.

At present, the variety of clinical diagnostic UC modalities mainly include imaging (ultrasound, computed tomography (CT), magnetic resonance imaging (MRI), intravenous urography), endoscopy examination and biopsy, urine cytology and tumor marker determination, etc. [8]. The advantages of imaging are noninvasive, simple and particularly suitable for the detection of larger tumors. The disadvantage is less sensitive for the diagnosis of small tumors, especially for carcinoma in situ [4]. Cystoscopy and ureteroscopy can clarify the location, number, shape and size of tumors, which is helpful to decide the next surgical plan, and biopsy of suspicious lesions can help clarify the diagnosis if necessary [9]. However, this method is an invasive examination, which may cause some pain to patients and cannot effectively identify carcinoma in situ and microscopic lesions, which may lead to misdiagnosis [10]. Urine exfoliative cytology is a noninvasive test commonly used in clinical practice for the diagnosis of UC, and although possessing a high specificity (85%–100%), it has a low sensitivity (28%–100%) [4]. Furthermore, it is often difficult to distinguish inflammatory lesions and epithelial atypical hyperplasia, which can result in a false positive rate of 1.3%–15% [11]. Fluorescence in situ hybridization (FISH), in general, has a relatively high specificity (28%–89%) and sensitivity (48%–88%) in the diagnosis of UC. However, the diagnostic sensitivity in low-grade tumors remains low (48%–61%), and its diagnostic criteria and overall performance vary from laboratory to laboratory, making it difficult to generalize [12, 13]. Therefore, there is an urgent need to find a simple, rapid, noninvasive and highly sensitive test to diagnose UC.

Tumor markers are tumor-related substances that can be detected in blood, body fluids and tissues, and the immunological properties of these substances can be used to determine and identify tumors, and reflect tumor occurrence, development and monitor tumor response to treatment [14]. Nuclear Matrix Protein 22 (NMP22) and bladder tumor antigen (BTA) are two tumor markers approved by the Food and Drug Administration (FDA) for the diagnosis of UC. A meta-analysis showed that their specificity and sensitivity were 76%, 79% and 68%, 67%, respectively [15]. However, their lower specificity and

higher false-positive rate limit the clinical use, because urinary tract infections and stones can affect the diagnostic specificity of NMP22 and BTA [15]. The current study found that a small class of single transmembrane proteins (FXVD3) was overexpressed in 90% of ureteral cancers and 84% of high-grade bladder cancers and in 40% of low-grade bladder cancers [16]. An analysis of FXVD3 levels in the urine of 30 UC patients found that FXVD3 levels were 69-fold and fourfold higher in high-grade UC and low-grade UC than in healthy groups, respectively [17]. However, this approach still cannot achieve ultrasensitive detection of FXVD3. Although FXVD3 can be used as a good specific biomarker for the detection of UC, there are very few studies on highly sensitive and specific biosensors for the detection of FXVD3 in urine.

Some technologies including polymerase chain reaction (PCR), enzyme-linked immunosorbent assay (ELISA) and colorimetric biosensing have attempted to detect FXVD3 [17–19]. However, the above methods were time-consuming, sophisticated and insensitive. With the advantages of fast response, high sensitivity, nondestructive and real-time monitoring, fluorescence analysis has been widely used by constructing various types of biosensing, particularly using near-infrared fluorescent nanoprobe [20]. Among them, NIR Ag<sub>2</sub>S quantum dots (Ag<sub>2</sub>S QDs) are widely used in the biomedical field because of their tunable spectrum, small size, high stability and good biocompatibility [21–24]. However, their low luminescence efficiency has limited their applications to a certain extent. Although the improvement of luminescence efficiency can be achieved by surface modification and assembly, the process is often lengthy [25]. A large number of studies have shown that the luminescence efficiency of fluorophores can be improved easily and effectively by localized surface plasmon resonance with precious metals [26–29].

Herein, we developed a plasmonic enhanced fluorescence based on the Ag<sub>2</sub>S QDs and gold nanorods (AuNRs) for sensitive detection and analysis of FXVD3, which were modified by monoclonal and polyclonal antibodies, respectively. As shown in Fig. 1, the AuNRs-polyclonal antibody 1 (AuNRs@Ab1) and Ag<sub>2</sub>S QDs-monoclonal antibody 2 (Ag<sub>2</sub>S@Ab2) were first obtained by Au–S bond and amination reaction, respectively. Then, the FXVD3 was first captured by Ag<sub>2</sub>S@Ab2 and then recognized by AuNRs@Ab1 to form a sandwich bioassay (AuNRs@Ab1-FXVD3-Ab2@Ag<sub>2</sub>S) with fluorescence enhancement. Importantly, this bioassay can be used to detect the FXVD3 in cancer urine samples with good sensitivity and specificity. Up to present, this is the first fluorescence-based bioassay to detect the FXVD3 in UC. Therefore, the designed sensor is expected to be used for UC screening, tumor grading and postoperative monitoring.

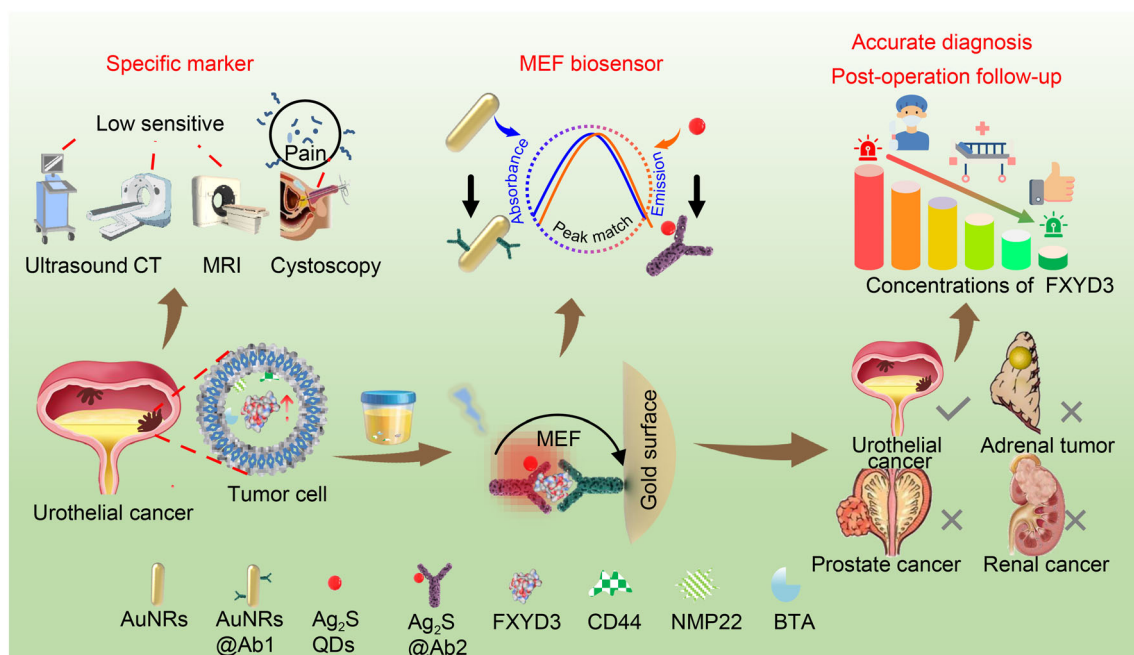


**Fig. 1** Schematic diagram of a fluorescent analysis method for detection of FXYD3 from UC based on AuNRs-enhanced NIR Ag<sub>2</sub>S QDs by metal-enhanced fluorescence (MEF)

## 2 Experimental

### 2.1 Reagents and materials

Gold (III) chloride trihydrate (HAuCl<sub>4</sub>·3H<sub>2</sub>O, 99.9 wt%), cetyltrimethylammonium bromide (CTAB, 99.0 wt%), (3-dimethylaminopropyl)-3-ethylcarbodiimide hydrochloride (EDC, 98 wt%) and N-hydroxysulfosuccinimide sodium salt (NHS, 97 wt%) were purchased from Sigma-Aldrich Co., Ltd. (Beijing, China). Sodium borohydride (NaBH<sub>4</sub>, 99.0 wt%), ascorbic acid (AA, 99.7 wt%), 3-mercaptopropionic acid (3-MPA, 98 wt%), silver nitrate (AgNO<sub>3</sub>, > 99.0 wt%), sodium hydroxide (NaOH, 99 wt%) and hydrochloric acid (HCl, 37 wt% in water) were obtained from Sinopharm Chemical Reagent Co., Ltd. (Shanghai, China). The recombinant human FXYD3 antigen, recombinant human CD44 protein, recombinant human NMP22 protein, recombinant human BTA, human FXYD3 ELISA kit and anti-FXYD3 polyclonal antibody were purchased from CRK Pharma Co., Ltd. (Wuhan, China). The anti-FXYD3 monoclonal antibody was purchased from Abcam (Shanghai, China). All chemicals were used without further purification.

### 2.2 Characterization

Ultraviolet–visible (UV–Vis) absorption spectra were collected on TU-180 UV–Vis spectrophotometer (Purkinje

General Instrument Co., Ltd.) (Shanghai, China). Transmission electron microscopy (TEM) was performed on JEOL HT-7700 electron microscope operating at 200 kV (Hitachi, Japan). Photoluminescence spectra were recorded on an Edinburgh FLS 980 fluorescence spectrophotometer (Edinburgh, England).

### 2.3 Synthesis of AuNRs

AuNRs were synthesized according to our previous reports with slight modification [30–34]. The process involves two steps: seed germination and growth. (1) Seed solution: 0.25 ml of 0.01 mol·L<sup>-1</sup> HAuCl<sub>4</sub> was mixed with 9.75 ml of 0.1 mol·L<sup>-1</sup> CTAB. Ice-cold NaBH<sub>4</sub> solution (0.01 mol·L<sup>-1</sup>, 0.60 ml) was then injected quickly into the mixture solution under vigorous stirred for 2 min and kept at 30 °C for at least 2 h for further use. (2) Growth solution: HAuCl<sub>4</sub> (0.01 mol·L<sup>-1</sup>, 0.5 ml), AgNO<sub>3</sub> (0.01 mol·L<sup>-1</sup>, 0.1 ml) and CTAB (0.10 mol·L<sup>-1</sup>, 10 ml) were added to a 15-ml glass bottle. After gentle mixing, 0.08 ml of 0.1 mol·L<sup>-1</sup> fresh AA solution was added, which resulted in the solution from dark yellow to transparent. Then, 0.2 ml of 1 mol·L<sup>-1</sup> HCl solution was added. The final step was that 20 μl of the seed solution was added to the growth solution, gently stirred for 10 s and standing at 30 °C for at least 6 h. AuNRs solution was centrifuged at 7500 r·min<sup>-1</sup> for 10 min and dispensed in deionized (DI) water.

## 2.4 Synthesis of AuNRs@Ab1

100  $\mu\text{l}$  of 2  $\mu\text{g}\cdot\text{ml}^{-1}$  FXYD3-Ab1 was added to 100  $\mu\text{l}$  of AuNRs and incubated at 37 °C for 30 min. AuNRs@FXYD3-Ab1 was purified by centrifugation (6500  $\text{r}\cdot\text{min}^{-1}$ , 8 min) and redispersed in 200  $\mu\text{l}$  phosphate buffer (PB) (0.01  $\text{mol}\cdot\text{L}^{-1}$ , pH 7.4) and stored at 4 °C.

## 2.5 Synthesis of Ag<sub>2</sub>S@Ab2

The aqueous synthesis of Ag<sub>2</sub>S QDs followed previous reports [21–23]. The carboxyl of Ag<sub>2</sub>S QDs was activated by EDC and NHS. Then, the amino group on the antibody surface formed an amide bond with the activated carboxyl group. 1 ml Ag<sub>2</sub>S QDs in 4 ml PB (0.01  $\text{mol}\cdot\text{L}^{-1}$ , pH 6.8) was activated by adding 5  $\mu\text{l}$  EDC and 5 mg NHS and stirred for 30 min at 30 °C. Then, 50  $\mu\text{l}$  of 2  $\mu\text{g}\cdot\text{ml}^{-1}$  FXYD3-Ab2 was added to 500  $\mu\text{l}$  activated Ag<sub>2</sub>S QDs and incubated at 37 °C for 30 min. The prepared Ag<sub>2</sub>S@Ab2 was kept at 4 °C for further use.

## 2.6 AuNRs@Ab1 and Ag<sub>2</sub>S@Ab2 for FXYD3 sensing

A sandwich structure consisting of AuNRs@Ab1-FXYD3-Ab2@Ag<sub>2</sub>S was performed as follows: predetermined amount of mixture of AuNRs@Ab1 (50  $\mu\text{l}$ , 0.25  $\text{nmol}\cdot\text{L}^{-1}$ ) and Ag<sub>2</sub>S@Ab2 (250  $\mu\text{l}$ , 2.28  $\text{mg}\cdot\text{ml}^{-1}$ ) was incubated together with different concentrations of FXYD3 antigen at 37 °C for 30 min, the final solution was adjusted to 2 ml by adding PB (0.01  $\text{mol}\cdot\text{L}^{-1}$ , pH = 7.4), and the fluorescence spectrum was recorded with the excitation of 468 nm. NMP22, BTA and CD44 were tested as possible interference substances, which was in order to research the specificity of the sandwich structure.

## 2.7 Sandwich structure for UC diagnosis

Fourteen patients diagnosed with UC by the pathological report were enrolled in our study. The clean catch mid-stream urine specimens from 10 patients with bladder tumor, 4 patients with UTUC, and 7 patients with other diseases were centrifuged at 2000  $\text{r}\cdot\text{min}^{-1}$  for 10 min at 4 °C. The precipitate was collected and stored at – 80 °C for further analyses. Freeze thawing (3 times) was used to split membranes and cell walls, and FXYD3 protein could be released. Then the urine samples were centrifuged again at 12,000  $\text{r}\cdot\text{min}^{-1}$  for 10 min at 4 °C before use and the supernatant was collected. AuNRs@Ab1 (50  $\mu\text{l}$ , 0.25  $\text{nmol}\cdot\text{L}^{-1}$ ) and Ag<sub>2</sub>S@Ab2 (250  $\mu\text{l}$ , 2.28  $\text{mg}\cdot\text{ml}^{-1}$ ), as well as 0.7 ml PB, were incubated together with 1 ml

urine sample at 37 °C for 30 min, and the fluorescence spectrum was recorded with the excitation of 468 nm. The written informed consent was approved by all patients, and this study was approved by the Institutional Ethical Committee of the Ningbo First Hospital (approval number: 2021-R114).

## 3 Results and discussion

### 3.1 Characteristics of AuNRs and Ag<sub>2</sub>S QDs

AuNRs were widely used in sensing fields due to its adjusted longitudinal plasmon resonance absorption peak from the ultraviolet region to the NIR region [35]. In this work, the prepared AuNRs (aspect ratio = 3.5) had uniform size and morphology with the average size of 18 nm in width and 63 nm in length and the maximum absorption peak was observed at 800 nm (Fig. 2a, b). At the same time, NIR Ag<sub>2</sub>S QDs with a maximum emission of 808 nm and an average particle size of 1.82 nm were also prepared (Fig. 2c, d). No absorption peak in the UV–Vis absorption spectrum for Ag<sub>2</sub>S QDs was observed due to its special electronic property [36]. All these preliminary data demonstrate the successful synthesis of AuNRs and Ag<sub>2</sub>S QDs. Moreover, the matching of the maximum absorption peak of AuNRs and the position of the maximum emission peak of NIR Ag<sub>2</sub>S provides a possible basis for plasmon resonance-enhanced fluorescence between the AuNRs and Ag<sub>2</sub>S QDs [37, 38].

### 3.2 Conjugation of AuNRs and Ag<sub>2</sub>S QDs with FXYD3-antibody

It is known that the protein has a characteristic UV absorption peak around 280 nm due to the presence of tryptophan [39]. Moreover, due to the presence of many different amino acids, protein structural molecules generally contain a large number of sulfhydryl (–SH) and amino (–NH<sub>2</sub>) functional groups [39]. Therefore, based on the Au–S bond, AuNRs were successfully labeled by Ab1 modification (Fig. 3a). As shown in Fig. 3c, AuNRs@Ab1 had a distinct protein characteristic absorption peak at 280 nm relative to the bare AuNRs. Similarly, Ab2 was successfully coupled to NIR Ag<sub>2</sub>S QDs based on the amidation reaction to obtain Ag<sub>2</sub>S@Ab2 (Fig. 3b, d), and the coupling of Ab2 did not negatively affect the fluorescence of Ag<sub>2</sub>S QDs (Fig. 3e). The successful modification of AuNRs and NIR Ag<sub>2</sub>S QDs by Ab1 and Ab2, respectively, laid the foundation for the subsequent specific detection of FXYD3.

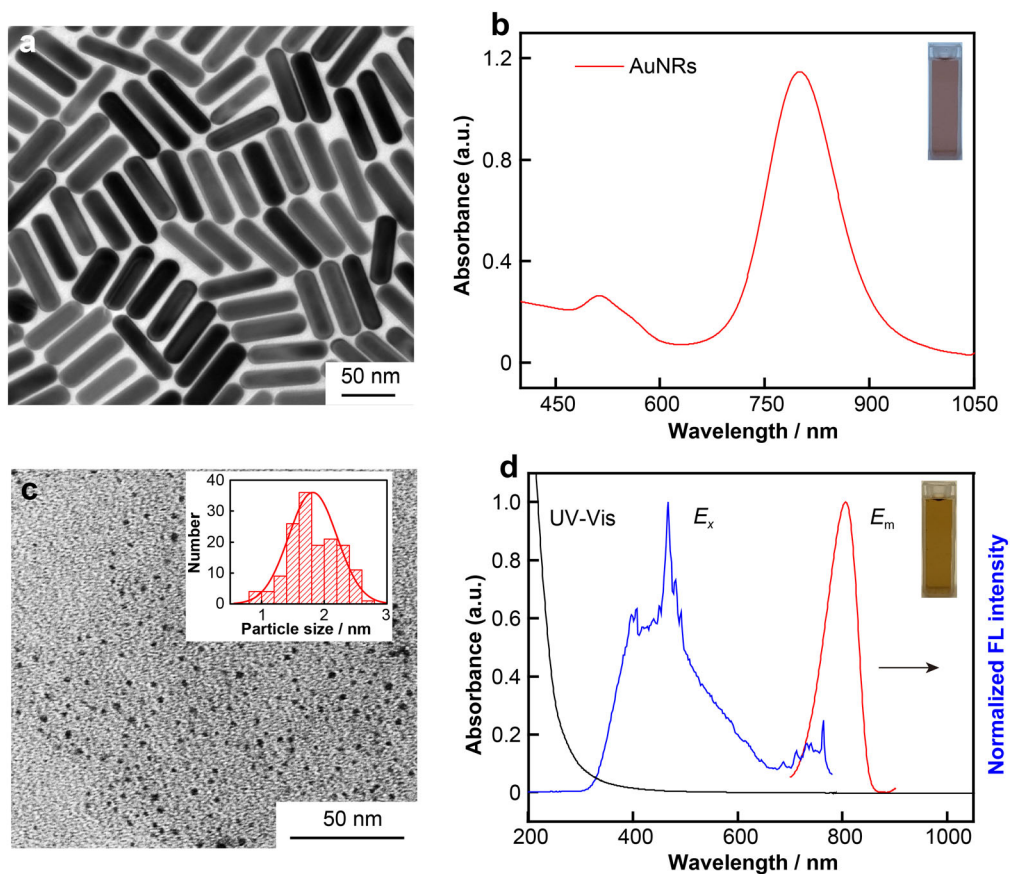


**Fig. 2** **a** TEM image of AuNRs; **b** UV-Vis absorption spectrum of AuNRs (inset being color of Au NRs in water, red brown); **c** TEM image of Ag<sub>2</sub>S QDs (inset: size distribution); **d** UV-Vis absorption spectrum (black line) and fluorescence spectrum (red line) of Ag<sub>2</sub>S QDs at excitation wavelength of 468 nm and the maximum emission ( $E_m$ ) is 808 nm (inset being color of Ag<sub>2</sub>S QDs in water, popcorn)

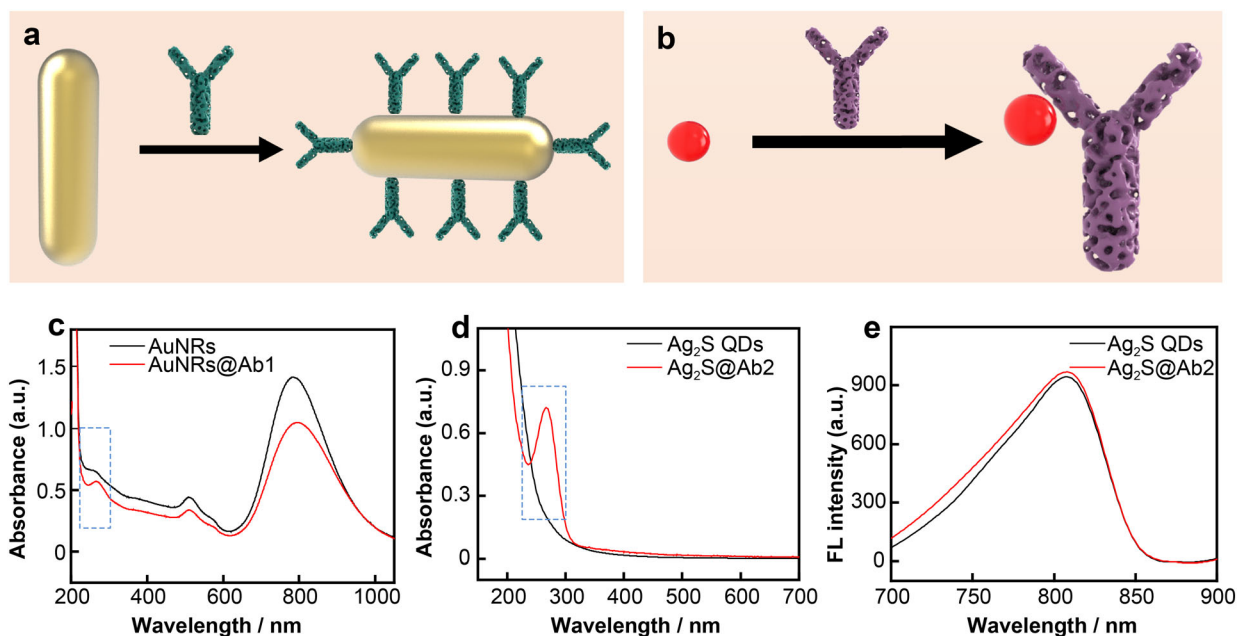


**Fig. 3** **a** Schematic diagram of AuNRs@Ab1; **b** schematic diagram of Ag<sub>2</sub>S QDs@Ab2; **c** UV-Vis absorption spectra of AuNRs (black line) and AuNRs@Ab1 (red line); **d**, **e** UV-Vis absorption spectra and fluorescence spectra of Ag<sub>2</sub>S QDs (black line) and Ag<sub>2</sub>S@Ab2 (red line)

### 3.3 Optimization of detection

Generally, the enhancement of fluorescence by precious metals is affected by the distance between particles and fluorescence molecules, and 5–30 nm is currently considered as an appropriate distance for fluorescence enhancement [40]. In this distance range, the electromagnetic field and radiation delay rate around the gold nanoparticles will increase, resulting in a substantial increase in fluorescence of the fluorophore [41]. However, there are also some other studies that show a good fluorescence enhancement effect with the other distance range. Luo et al. found that 15 nm and 34 nm of silica shell on AuNPs had less fluorescence enhancement compared with the 22 nm with fivefold enhancement [41]. Niu et al. [42] showed that the Au nanobipyramids@SiO<sub>2</sub>@Cyanine7 NPs reached the best enhancement factor (10.7) at approximately 17 nm of silica shell. The molecular weights of antibody and antigen are 150 and 27.8 kDa, corresponding to sizes of about 10 and 2 nm, respectively [43]. The linear length of the AuNRs@Ab1-FXYD3-Ab2@Ag<sub>2</sub>S sandwich structure can be theoretically deduced to be about 12 nm. At this distance, there will still be some plasmon resonance enhance fluorescence. In our study, although the distance between AuNRs and Ag<sub>2</sub>S QDs could not be modulated, we further optimized the concentrations of AuNRs and Ag<sub>2</sub>S QDs to improve the sensitivity of FXYD3 detection to some extent. Because the AuNRs@Ab1-FXYD3-Ab2@Ag<sub>2</sub>S can be viewed as core-shell-satellite structure that binds multiple receptors, the fluorescence enhancement factor was calculated by the ratio of fluorescence intensity of AuNRs@Ab1-FXYD3-Ab2@Ag<sub>2</sub>S QDs to the fluorescence intensity of bare Ag<sub>2</sub>S QDs combined with AuNRs at the same concentrations of QDs. As shown in Fig. S1a–c and Fig. S2a, b, the best enhancement factor (2.9) was obtained at the concentrations of 0.5 nmol·L<sup>-1</sup> AuNRs and 285 μg·ml<sup>-1</sup> Ag<sub>2</sub>S QDs.

### 3.4 Sensitive and specific detection of FXYD3

Under the optimized condition, AuNRs@Ab1 and Ag<sub>2</sub>S@Ab2 were used for the analysis of FXYD3 detection (Fig. 4a). As shown in Fig. 4b, c, the fluorescence of Ag<sub>2</sub>S@Ab2 was enhanced with increasing concentrations of FXYD3 (0.25–300 ng·ml<sup>-1</sup>). A good linear relationship was observed between the concentrations of FXYD3 in the range of 0.25–150 ng·ml<sup>-1</sup>, with a detection limit of 0.2 ng·ml<sup>-1</sup> (Fig. 4d). Based on the previous report, the concentrations of FXYD3 from low-grade and high-grade UC urine samples are (7.23 ± 2.35) and (30.72 ± 18.32) ng·ml<sup>-1</sup>, respectively. Therefore, this biosensor can be used to directly detect the real urine sample of the UC. Additionally, the specificity of sandwich biosensor for

recognizing the FXYD3 was further studied by comparing with the possible interfering molecules (CD44, BTA, and NMP22) (Fig. 4a). The results of Fig. 4e showed that the fluorescence intensity of CD44, BTA and NMP22 was similar to the control group, while the FXYD3 group showed an obvious enhancement when the concentrations of FXYD3 were 100 ng·ml<sup>-1</sup>. These results proved that the sandwich biosensor had excellent sensitivity and remarkable specificity for the detection of FXYD3.

To further demonstrate visually the different fluorescence intensities of AuNRs@Ab1-FXYD3-Ab2@Ag<sub>2</sub>S sandwich, the experimental results are investigated using the specific binding of different concentrations of FXYD3. TEM images of AuNRs@Ab1-FXYD3-Ab2@Ag<sub>2</sub>S at different concentrations of FXYD3 are shown in Fig. 5. Remarkably, the different numbers of Ag<sub>2</sub>S@Ab2 QDs surrounding AuNRs@Ab1 can be intuitively observed. With the increase in concentrations of FXYD3, more Ag<sub>2</sub>S@Ab2 QDs can be attached to the AuNRs@Ab1 (Fig. 5a–c). In other words, compared with the low concentrations of FXYD3, the high concentrations of FXYD3 made the AuNRs@Ab1 recognize the more Ag<sub>2</sub>S QDs@Ab2 with stronger fluorescence enhancement (Fig. 5d).

### 3.5 Detecting FXYD3 in different samples

To further validate the application of this biosensor in real sample detection, the reliability was further verified by adding different concentrations of FXYD3 to PB and urine samples. As shown in Table 1, the spiked recoveries ranged from 97.26% to 101.80%. All recoveries were within the range of reliable detection, indicating the potential application of this biosensor in real sample detection.

Encouraged by the outcomes above, urine samples including 10 bladder tumor patients (7 patients diagnose with high-grade UC, 3 patients diagnosed with low-grade UC), 4 UTUC patients (high-grade UC) and 7 patients with other diseases were collected. Based on the cystoscopy, 12.5% (2/16) patients would suffer from surgery, and two of these patients diagnosed with bladder tumor by cystoscopy were chronic cystitis (confirmed by pathology). If this biosensor can be applied to directly detect the FXYD3 in cancer sample for UC diagnosis and tumor-grade classification, 12.5% (2/16) patients will avoid the pain caused by overtreatment. All the results are shown in Table 2, and the mean concentration of FXYD3 was 0.73 ng·ml<sup>-1</sup> in the control group. The mean concentrations of FXYD3 were 57.32 and 8.60 ng·ml<sup>-1</sup> in high-grade UC and low-grade UC, respectively, which have an approximately 78-fold and 12-fold overexpression than control group (Fig. S3). In all, the diagnostic results obtained from this fluorescence sensing of FXYD3 expression levels were consistent with

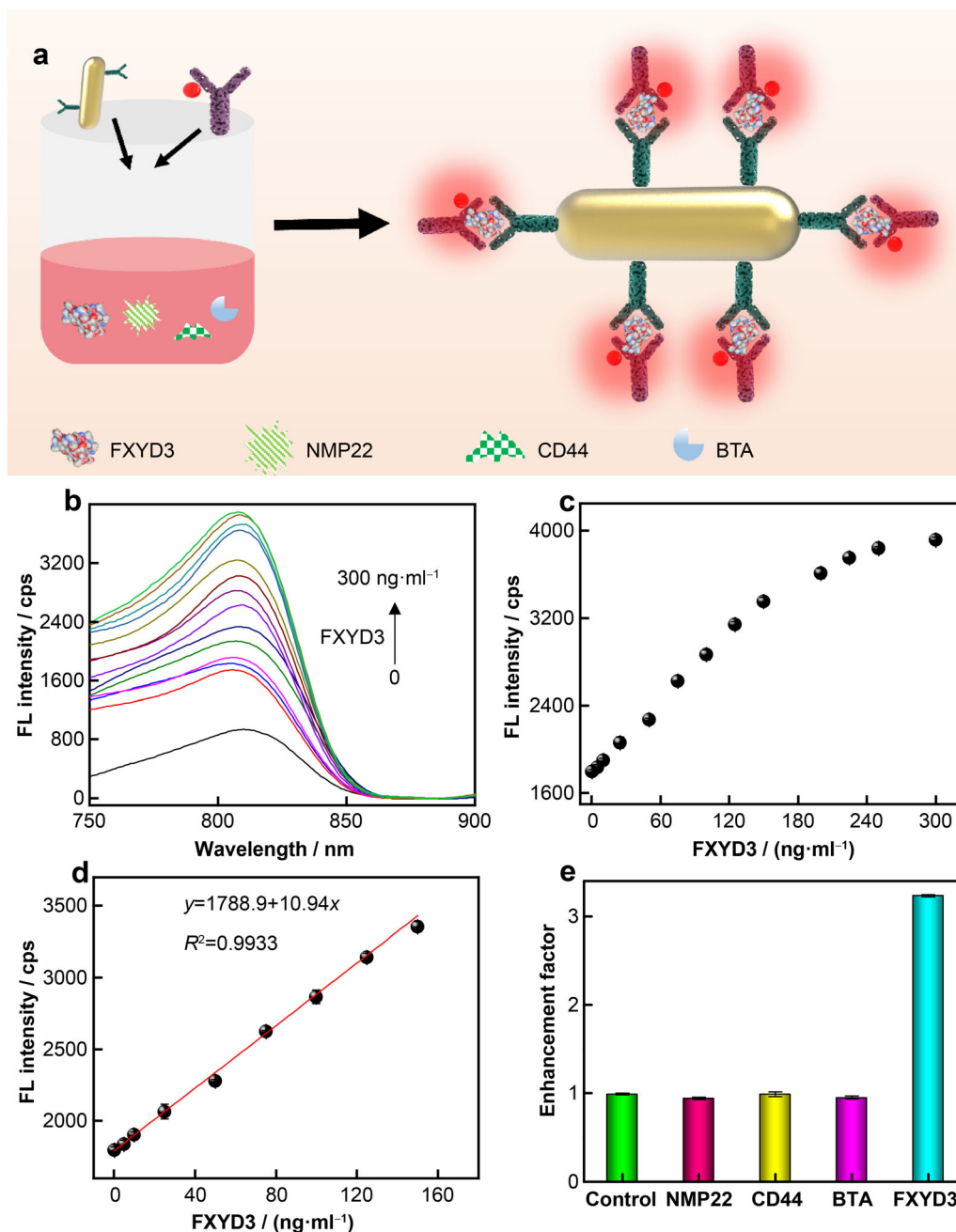


**Fig. 4** **a** Schematic diagram of sandwich biosensor specificity; **b** fluorescence spectra of sandwich biosensor with different concentrations of FXYD3 at excitation wavelength of 468 nm (concentrations of FXYD3 from low to high were 0, 0.25, 5, 10, 25, 50, 75, 100, 125, 150, 200, 225, 250, 300 ng·ml<sup>-1</sup>); **c** relationship between fluorescence intensity and concentration of FXYD3; **d** calibration curve of sandwich biosensor for detection of FXYD3, where error bars were obtained from three parallel experiments; **e** enhancement factor of Ag<sub>2</sub>S@Ab<sub>2</sub> and AuNRs@Ab<sub>1</sub> incubated with different target antigens

the tumor grade confirmed by clinical cystoscopy as well as pathology. This indicates that this fluorescent biosensor is expected to be used for the diagnosis and identification of UC in the clinical setting.

Next, the fluorescent biosensor is applied for postoperative monitoring. The urine of two high-grade UC was collected again at 3 months postoperatively (high-grade

UTUC and high-grade bladder cancer with number 4), in which the concentrations of FXYD3 decreased from 93.54 and 93.50 ng·ml<sup>-1</sup> to 0.55 and 3.12 ng·ml<sup>-1</sup> by ELISA kit, respectively. And no recurrence phenomenon was observed by imaging and cystoscopy. The same results were also accurately quantified and determined by this fluorescent biosensor (0.52 and 3.55 ng·ml<sup>-1</sup>). And at the same time,

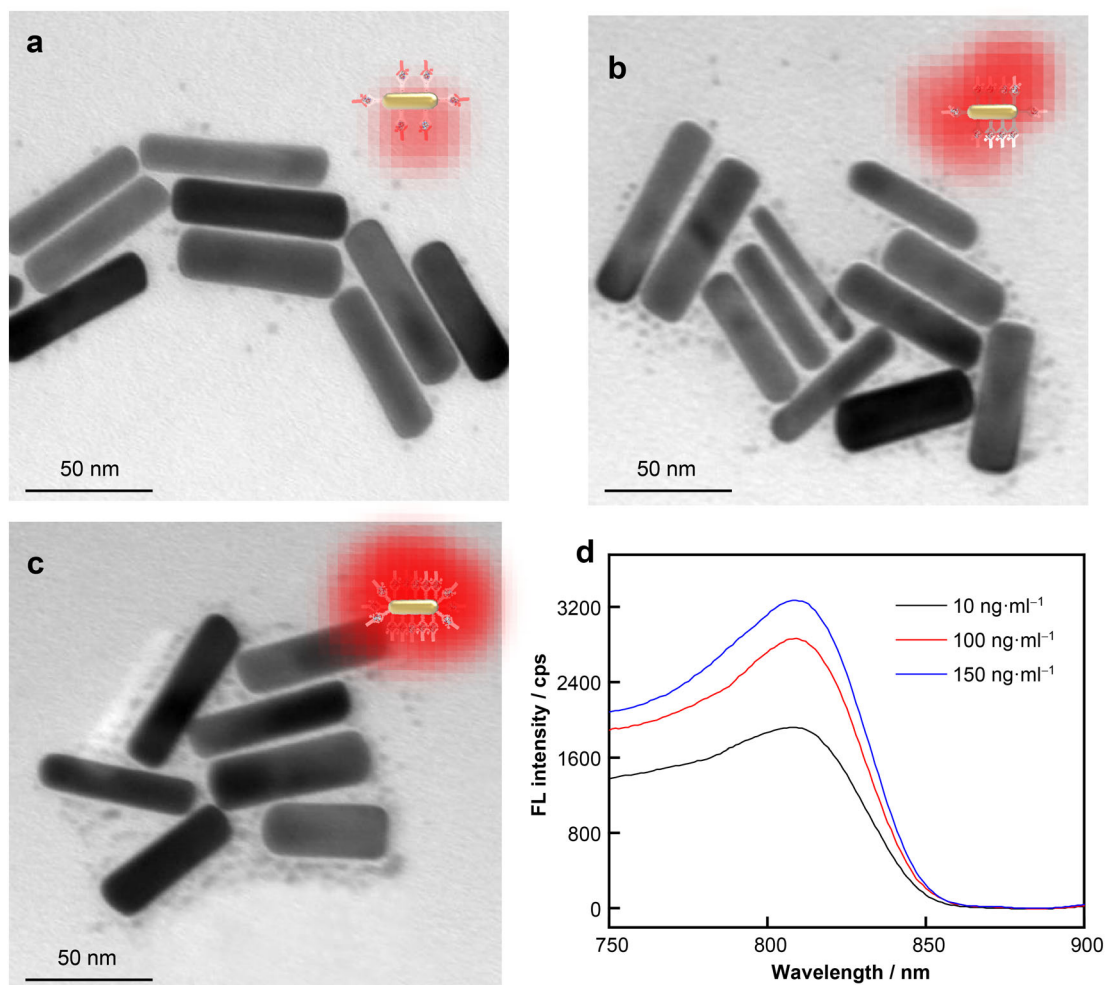


**Fig. 5** TEM images of AuNRs@Ab1-FXYD3-Ab2@Ag<sub>2</sub>S with different concentrations of FXYD3: **a** 10 ng·ml<sup>-1</sup>, **b** 100 ng·ml<sup>-1</sup>, **c** 150 ng·ml<sup>-1</sup> (inset: schematic diagram); **d** corresponding fluorescence spectra of sandwich biosensors with different concentrations of FXYD3 at excitation wavelength of 468 nm

**Table 1** Analytical results of FXYD3 in PB and urine samples

Samples	Concentration / (ng·ml <sup>-1</sup> )	Fluorescence / (ng·ml <sup>-1</sup> )	Recovery / %
PB	10	10.15 ± 0.41	101.5
	50	48.63 ± 0.61	97.26
	125	124.97 ± 1.67	99.98
Human urine	10	10.18 ± 0.45	101.80
	50	49.07 ± 0.84	98.14
	125	124.40 ± 3.25	99.52

one patient (high-grade bladder cancer with number 4) that the concentration of FXYD3 drop to 3.55 ng·ml<sup>-1</sup> need to be monitored every 3 months. If the FXYD3 level continues to rise, imaging and cystoscopy should be performed. Collectively, this fluorescent biosensor can be used to rapidly monitor FXYD3 expression levels in urine in

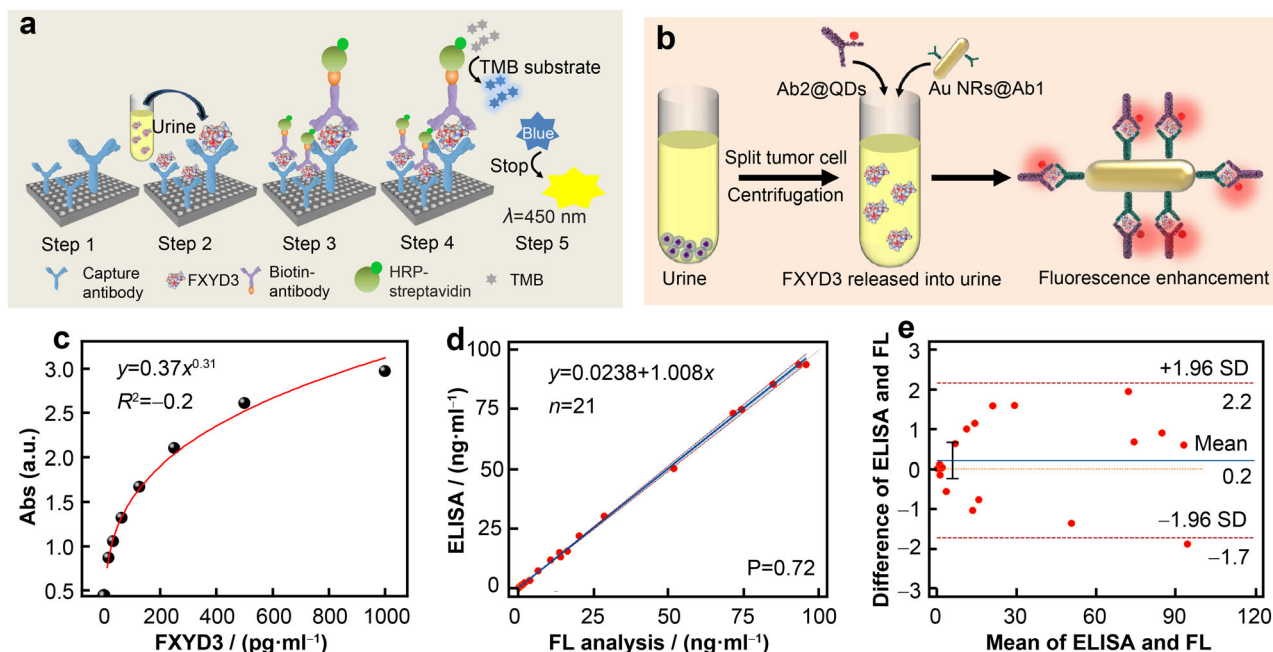
real time to inform patients to avoid unnecessary imaging and cystoscopy.

To further prove the reliability of the fluorescent biosensor as a clinical tool in UC diagnosis, the sandwich bioassay results for 21 urine samples were compared with ELISA assay. The schematic diagrams of two methods to detect FXYD3 in urine are shown in Fig. 6a, b. Firstly, the standard curve of FXYD3 obtained from ELISA kit is shown in Fig. 6c. Then the Passing–Bablok regression analysis revealed a slope of 1.008 (95% confidence interval (CI), 0.98 to 1.03) and an ordinate intercept of 0.02 (95% CI 0.02 to 0.07) in Fig. 6d and Table S1. And the good conformity between two methods ( $P = 0.7$ ) further demonstrated that the reliability of this fluorescent biosensor. In addition, Bland–Altman plot showed the 1/21 (< 5%) of points were outside of 95% limits of agreement, indicating the excellent conformity between two methods once again (Fig. 6e) while compared with ELISA assay,



**Table 2** Behavior of cystoscopy, pathology and FXYD3 in detecting UC

Patients	Number	Cystoscopy	Pathology	FXYD3	ELISA assay / (ng·ml <sup>-1</sup> )	Fluorescence assay / (ng·ml <sup>-1</sup> )
High grade UTUC	1	Positive	Positive	Positive	74.70	74.02
	2	Positive	Positive	Positive	21.80	20.22
	3	Positive	Positive	Positive	30.07	28.48
	4	Positive	Positive	Positive	93.54	95.42
High grade bladder cancer	1	Positive	Positive	Positive	11.66	10.66
	2	Positive	Positive	Positive	85.38	84.48
	3	Positive	Positive	Positive	50.14	51.50
	4	Positive	Positive	Positive	93.50	92.90
	5	Positive	Positive	Positive	73.14	71.20
	6	Positive	Positive	Positive	12.96	14.00
Low grade bladder cancer	1	Positive	Positive	Positive	3.18	3.74
	2	Positive	Positive	Positive	7.17	6.54
	3	Positive	Positive	Positive	15.45	16.22
Prostate cancer	1	Negative	Negative	Negative	2.02	1.98
Adrenal adenoma	1	Negative	Negative	Negative	1.15	1.04
	2	Negative	Negative	Negative	1.24	1.24
Renal tumor	1	Negative	Negative	Negative	0.25	0.24
Pelvic tumor	1	Negative	Negative	Negative	0.87	0.82
Cystitis	1	Positive	Negative	Negative	1.19	1.34
	2	Positive	Negative	Negative	0.21	0.20
High grade UTUC (postoperative)	4	Negative	Not available	Negative	0.55	0.52

**Fig. 6** a, b Schematic diagram of detecting FXYD3 by ELISA and this fluorescence biosensor; c standard curve of FXYD3 assay obtained by ELISA kit; d, e Passing–Bablok regression analyses and Bland–Altman plot between ELISA Kit and fluorescence analysis

our method improved the detection speed and accuracy. In summary, this fluorescent biosensor enables real-time rapid and accurate monitoring of FXYD3 expression levels in urine for cancer determination, tumor-grade classification and postoperative monitoring.

#### 4 Conclusion

In summary, we developed a simple fluorescent biosensor for fast and accurate detection of FXYD3 in the urine of cancer patients by plasmon-enhanced fluorescence. A good linear relationship was obtained between the concentrations of FXYD3 in the range of 0.25–150 ng·ml<sup>-1</sup>, with a detection limit of 0.2 ng·ml<sup>-1</sup>. All results demonstrate the high sensitivity, specificity and accuracy of this simple fluorescent biosensor. Importantly, the approximate results obtained with 21 urine samples by the ELISA kit and this fluorescent biosensor endows it with certain practical potential. Namely, this fast, ultrasensitive and precise fluorescent biosensor is expected to be used for UC screening, tumor-grade classification and postoperative monitoring.

**Acknowledgements** This work was financially supported in part by the National Natural Science Foundation of China (Nos. 22005081, 51873222 and 52111530128), Zhejiang Provincial Natural Science Foundation of China (Nos. LY22B050003 and LZ22B050001), the Funding for the Scientific Research Foundation for Scholars of Hangzhou Normal University (Nos. 4095C5021920467 and 4095C5021920452), and the Key Research and Development Projects of Anhui Province (Nos. 202004g01020016 and 202104g01020009).

#### Declarations

**Conflict of interests** The authors declare that they have no conflict of interest.

#### References

- [1] Crabb SJ. Treatment of upper urinary tract urothelial carcinoma. *Lancet*. 2020;395:1232. [https://doi.org/10.1016/S01406736\(20\)30519-5](https://doi.org/10.1016/S01406736(20)30519-5).
- [2] Ottley EC, Pell R, Brazier B, Hollidge J, Kartsonaki C, Browning L, O'Neill E, Kiltie AE. Greater utility of molecular subtype rather than epithelial-to-mesenchymal transition (EMT) markers for prognosis in high-risk non-muscle-invasive (HGT1) bladder cancer. *J Pathol Clin Res*. 2020;6(4):238. <https://doi.org/10.1002/cjp2.167>.
- [3] Zhang D, Yao LF, Yu S, Cheng Y, Jiang JH, Ma Q. Safety and efficacy of en bloc transurethral resection versus conventional transurethral resection for primary nonmuscle-invasive bladder cancer: a meta-analysis. *World J Surg Onc*. 2020;18(1):1. <https://doi.org/10.21203/rs.2.11157/v1>.
- [4] Babjuk M, Burger M, Comp erat EM, Gontero P, Mostafid AH, Palou J, van Rhijn BWG, Roup r t M, Shariat SF, Sylvester R, Zigeuner R, Capoun O, Cohen D, Escrig JLD, Hern andez V, Peyronnet B, Seisen T, Soukup V. European association of urology guidelines on non-muscle-invasive bladder cancer (TaT1 and carcinoma in situ)-2019 update. *Eur Urol*. 2019;76(5):639. <https://doi.org/10.1016/j.eururo.2019.08.016>.
- [5] Witjes JA, Bruins HM, Cathomas RL, Comp erat EM, Cowan NC, Gakis G, Hern andez V, Linares Espin os E, Lorch A, Neuzillet Y, Rouanne M, Thalmann GN, Veskim e E, Ribal MJ, van der Heijden AG. European association of urology guidelines on muscle-invasive and metastatic bladder cancer: summary of the 2020 guidelines. *Eur Urol*. 2020;79(1):82. <https://doi.org/10.1016/j.eururo.2020.03.055>.
- [6] Roup r t M, Babjuk M, Burger M, Capoun O, Cohen D, Comp erat EM, Cowan NC, Dom nguez-Escrig JL, Gontero P, Hugh Mostafid A, Palou J, Peyronnet B, Seisen T, Soukup V, Sylvester RJ, Rhijn BWGV, Zigeuner R, Shariat SF. European association of urology guidelines on upper urinary tract urothelial carcinoma: 2020 update. *Eur Urol*. 2020;79(1):62. <https://doi.org/10.1016/j.eururo.2020.05.042>.
- [7] Soria F, Shariat SF, Lerner SP, Fritsche HM, Rink M, Kassouf W, Spiess PE, Lotan Y, Ye D, Fern andez MI, Kikuchi E, Chade DC, Babjuk M, Grollman AP, Thalmann GN. Epidemiology, diagnosis, preoperative evaluation and prognostic assessment of upper-tract urothelial carcinoma (UTUC). *World J Urol*. 2017;35(3):379. <https://doi.org/10.1007/s00345-016-1928-x>.
- [8] Babjuk M, Burger M, Capoun O, Cohen D, Comp erat EM, Dom nguez Escrig J, Gontero P, Liedberg F, Masson-Lecomte A, Mostafid AH, Palou J, van Rhijn BWG, Roup r t M, Shariat SF, Seisen T, Soukup V, Sylvester RJ. European association of urology guidelines on non-muscle-invasive bladder cancer (Ta, T1, and carcinoma in situ). *Eur Urol*. 2022;81(1):75. <https://doi.org/10.1016/j.eururo.2021.08.010>.
- [9] Huang HM, Li HX. Tumor heterogeneity and the potential role of liquid biopsy in bladder cancer. *Cancer Commun*. 2021;41(2):91. <https://doi.org/10.1002/cac2.12129>.
- [10] Kamat AM, Hahn NM, Efstathiou JA, Lerner SP, Malmstr m P, Choi W, Guo CC, Lotan Y, Kassouf W. Bladder cancer. *The Lancet*. 2016;388(10061):2796. [https://doi.org/10.1016/S0140-6736\(16\)30512-8](https://doi.org/10.1016/S0140-6736(16)30512-8).
- [11] Xing J, Reynolds JP. Diagnostic advances in urine cytology. *Surg Pathol Clin*. 2018;11(3):601. <https://doi.org/10.1016/j.path.2018.06.001>.
- [12] McIntire PJ, Khan R, Hussain H, Pambuccian SE, Wojcik EM, Barkan GA. Negative predictive value and sensitivity of urine cytology prior to implementation of the paris system for reporting urinary cytology. *Cancer Cytopathol*. 2019;127(2):125. <https://doi.org/10.1002/cncy.22102>.
- [13] Sun T, Hutchinson L, Tomaszewicz K, Caporelli ML, Meng X, Mccauley K, Fischer AH, Cosar EF, Cornejo KM. Diagnostic value of a comprehensive, urothelial carcinoma-specific next-generation sequencing panel in urine cytology and bladder tumor specimens. *Cancer Cytopathol*. 2021;129(7):537. <https://doi.org/10.1002/cncy.22410>.
- [14] Tang Z, Ma Z. Multiple functional strategies for amplifying sensitivity of amperometric immunoassay for tumor markers: a review. *Biosens Bioelectron*. 2017;98:100. <https://doi.org/10.1016/j.bios.2017.06.041>.
- [15] Sathianathen NJ, Butaney M, Weight CJ, Kumar R, Konety BR. Urinary biomarkers in the evaluation of primary hematuria: a systematic review and meta-analysis. *Bladder Cancer*. 2018;4(4):353. <https://doi.org/10.3233/BLC-180179>.
- [16] Zhang ZF, Pang ST, Kasper KA, Luan C, Wondergem B, Lin F, Chuang CK, The BT, Yang XJ. FXYD3: a promising biomarker for urothelial carcinoma. *Biomarker Insights*. 2011;6(6):17. <https://doi.org/10.4137/bmi.s6487>.
- [17] Hsu YP, Yang HW, Li NS, Chen YT, Pang ST. Instrument-free detection of FXYD3 using vial based immunosensor for earlier



- and faster urothelial carcinoma diagnosis. *ACS Sens.* 2020;5(4): 928. <https://doi.org/10.1021/acssensors.9b02013>.
- [18] Laura L, Mengual L, Gazquez C, Ingelmo-Torres M, Alcaraz A. Molecular characterization of upper urinary tract tumours. *BJU Int.* 2010;9(6):260. [https://doi.org/10.1016/S1569-9056\(10\)60796-8](https://doi.org/10.1016/S1569-9056(10)60796-8).
- [19] Gazquez C, Ribal M, Marín-Aguilera M, Kayed H, Fernández P, Mengual L, Alcaraz A. Biomarkers vs conventional histological analysis to detect lymph node micrometastases in bladder cancer: a real improvement. *BJU Int.* 2012;110(9):1310. <https://doi.org/10.1111/j.1464-410x.2012.11025.x>.
- [20] Wu L, Liu J, Li P, Tang B, James TD. Two-photon small-molecule fluorescence-based agents for sensing, imaging, and therapy within biological systems. *Chem Soc Rev.* 2021;50(2): 702. <https://doi.org/10.1039/d0cs00861c>.
- [21] Ding CP, Zhang CL, Cheng SS, Xian YZ. Multivalent aptamer functionalized Ag<sub>2</sub>S nanodots/hybrid cell membrane-coated magnetic nanobioprobe for the ultrasensitive isolation and detection of circulating tumor cells. *Adv Funct Mater.* 2020; 30(16):28732. <https://doi.org/10.1002/adfm.201909781>.
- [22] Ding CP, Huang YJ, Shen ZY, Chen XY. Synthesis and bioapplications of Ag<sub>2</sub>S quantum dots with near-infrared fluorescence. *Adv Mater.* 2021;33(32):2007768. <https://doi.org/10.1002/adma.202007768>.
- [23] Ding CP, Cheng SS, Zhang CL, Xiong YR, Ye MQ, Xian YZ. Ratiometric upconversion luminescence nanoprobe with near-infrared Ag<sub>2</sub>S nanodots as the energy acceptor for sensing and imaging of pH in vivo. *Anal Chem.* 2019;91(11):7181. <https://doi.org/10.1021/acs.analchem.9b00404>.
- [24] Ding CP, Zhang CL, Yin XY, Cao XY, Cai MF, Xian YZ. Near-infrared fluorescent Ag<sub>2</sub>S nanodot-based signal amplification for efficient detection of circulating tumor cells. *Anal Chem.* 2018;90(11):6702. <https://doi.org/10.1021/acs.analchem.8b00514>.
- [25] Senellart P, Solomon G, White A. High-performance semiconductor quantum-dot single-photon sources. *Nat Nanotechnol.* 2017;12(11):1026. <https://doi.org/10.1038/nnano.2017.218>.
- [26] Choi JH, Ha T, Shin M, Lee SN, Choi JW. Nanomaterial-based fluorescence resonance energy transfer (FRET) and metal-enhanced fluorescence (MEF) to detect nucleic acid in cancer diagnosis. *Biomedicines.* 2021;9(8):928. <https://doi.org/10.3390/biomedicines9080928>.
- [27] Liang ZC, Hao CL, Chen C, Ma W, Sun MZ, Xu LG, Xu C, Kuang H. Ratiometric FRET encoded hierarchical ZrMOF@Au cluster for ultrasensitive quantifying microRNA in vivo. *Adv Mater.* 2021;34:2107449. <https://doi.org/10.1002/adma.202107449>.
- [28] Chai S, Lv WY, He JH, Li CH, Huang CZ. Dual energy transfers-based fluorescent nanoprobe for imaging miR-21 in non-alcoholic fatty liver cells with low background. *Anal Chem.* 2019;91(10):6761. <https://doi.org/10.1021/acs.analchem.9b00841>.
- [29] Wang JC, Luo HS, Zhang MH. Design and fabrication of a new fluorescence enhancement system of silver nanoparticles-decorated aligned silver nanowires. *Rare Met.* 2019;38(12):1178. <https://doi.org/10.1007/s12598-019-01275-6>.
- [30] Song LP, Qiu NX, Huang JY, Cheng Q, Yang YP, Lin H, Su FM, Chen T. Macroscopic orientational gold nanorods monolayer film with excellent photothermal anticounterfeiting performance. *Adv Opt Mater.* 2020;8(18):1902082. <https://doi.org/10.1002/adom.201902082>.
- [31] Lin H, Song LP, Huang YJ, Cheng Q, Chen T. Macroscopic Au@PANI core/shell nanoparticle superlattice monolayer film with dual-responsive plasmonic switches. *ACS Appl Mater Inter.* 2020;12(9):11296. <https://doi.org/10.1021/acsaami.0c01983>.
- [32] Fang BL, Xu SH, Huang YJ, Su FM, Huang Z, Fang H, Peng J, Xiong Y, Lai W. Gold nanorods etching-based plasmonic immunoassay for qualitative and quantitative detection of aflatoxin M1 in milk. *Food Chem.* 2020;329:127160. <https://doi.org/10.1016/j.foodchem.2020.127160>.
- [33] Song LP, Chen J, Xu BB, Huang YJ. Flexible plasmonic biosensors for healthcare monitoring: progress and prospects. *ACS Nano.* 2021;15(12):18822. <https://doi.org/10.1021/acsnano.1c07176>.
- [34] Song LP, Xu BB, Cheng Q, Wang XY, Luo XN, Chen X, Chen T, Huang YJ. Instant interfacial self-assembly for homogeneous nanoparticle monolayer enabled conformal “lift-on” thin film technology. *Sci Adv.* 2021;7:eabk2852. <https://doi.org/10.1126/sciadv.abk2852>.
- [35] Liang C, Luan JY, Wang ZY, Jiang QS, Gupta R, Cao SS, Liu KK, Morrissey JJ, Kharasch ED, Naik RR, Singamaneni S. Gold nanorod size-dependent fluorescence enhancement for ultrasensitive fluorimmunoassays. *ACS Appl Mater Interfaces.* 2021; 13(9):11414. <https://doi.org/10.1021/acsaami.0c20303>.
- [36] Zhang YJ, Liu YS, Li CY, Chen XY, Wang QB. Controlled synthesis of Ag<sub>2</sub>S quantum dots and experimental determination of the exciton bohr radius. *J Phys Chem C.* 2014;118:4918. <https://doi.org/10.1021/jp501266d>.
- [37] Mei Z, Tang L. Surface-plasmon-coupled fluorescence enhancement based on ordered gold nanorod array biochip for ultrasensitive DNA analysis. *Anal Chem.* 2017;89(1):633. <https://doi.org/10.1021/acs.analchem.6b02797>.
- [38] Abadeer NS, Brennan MR, Wilson WL, Murphy CJ. Distance and plasmon wavelength dependent fluorescence of molecules bound to silica-coated gold nanorods. *ACS Nano.* 2014;8(8): 8392. <https://doi.org/10.1021/nn502887j>.
- [39] Starosta R, Santos FC, Almeida R. Human and bovine serum albumin time-resolved fluorescence: tryptophan and tyrosine contributions, effect of DMSO and rotational diffusion. *J Mol Struct.* 2020;1221: 128805. <https://doi.org/10.1016/j.molstruc.2020.128805>.
- [40] Choi JH, Choi JW. Metal-enhanced fluorescence by bifunctional Au nanoparticles for highly sensitive and simple detection of proteolytic enzyme. *Nano Lett.* 2020;20(10):7100. <https://doi.org/10.1021/acs.nanolett.0c02343>.
- [41] Luo Y, Song Y, Zhu C, Li S, Xian M, Wai CM, Lin Y, Du D. Visualization of endogenous hydrogen sulfide in living cells based on Au nanorods@silica enhanced fluorescence. *Anal Chim Acta.* 2018;1053:81. <https://doi.org/10.1016/j.aca.2018.12.008>.
- [42] Niu C, Song Q, He G, Na N, Ouyang J. Near-infrared-fluorescent probes for bioapplications based on silica-coated gold nanobipyramids with distance-dependent plasmon-enhanced fluorescence. *Anal Chem.* 2016;88(22):11062. <https://doi.org/10.1021/acs.analchem.6b03034>.
- [43] Wegner KD, Jin Z, Lindén S, Jennings TL, Hildebrandt N. Quantum-dot-based Förster resonance energy transfer immunoassay for sensitive clinical diagnostics of low-volume serum samples. *ACS Nano.* 2013;7(8):7411. <https://doi.org/10.1021/nn403253y>.